Verifying single-station seismic approaches using Earth-based data: Preparation for data return from the InSight mission to Mars

Mark P. Panning[a], Éric Beucler[b], Mélanie Drilleau[b,c], Antoine Mocquet[b], Philippe Lognonné[c], W. Bruce Banerdt[d]

[a]*Department of Geological Sciences, University of Florida*
[b]*Laboratoire de Planétologie et Géodynamique, Université de Nantes*
[c]*Univ Paris Diderot-Sorbonne Paris Cité, Institut de Physique du Globe Paris*
[d]*Jet Propulsion Laboratory, California Institute of Technology*

Abstract

The planned InSight mission will deliver a single seismic station containing 3-component broadband and short-period sensors to the surface of Mars in 2016. While much of the progress in understanding the Earth and Moon's interior has relied on the use of seismic networks for accurate location of sources, single station approaches can be applied to data returned from Mars in order to locate events and determine interior structure. In preparation for the data return from InSight, we use a terrestrial dataset recorded at the Global Seismic Network station BFO, located at the Black Forest Observatory in Germany, to verify an approach for event location and structure determination based on recordings of multiple orbit surface waves, which will be more favorable to record on Mars than Earth due to smaller planetary radius and potentially lower background noise. With this approach applied to events near the threshold of observability on Earth, we are able to determine epicentral distance within approximately 1 degree (corresponding to ∼60 km on Mars), and origin time within ∼30 seconds. With back azimuth determined from Rayleigh wave polarization, absolute locations are determined generally within an aperture of 10 degrees, allowing for localization within large tectonic regions on Mars. With these locations, we are able to recover Earth mantle structure within ±5% (the InSight mission requirements for Martian mantle structure) using 1D travel time inversions of P and S travel times for datasets of only 7 events. The location algorithm also allows for the measurement of great-circle averaged group velocity dispersion, which we

measure between 40 and 200 seconds to scale the expected reliable frequency range of the Insight data from Earth to Mars data. Using the terrestrial data, we are able to resolve structure down to ∼200 km, but synthetic tests demonstrate we should be able to resolve Martian structure to ∼400 km with the same frequency content given the smaller planetary size.

Key words: Mars, interior, Geophysics, Earth

1. Introduction

Seismology is one of the strongest observational tools available in order to constrain the deep interior structure of planetary bodies (Lognonné and Johnson, 2007). After the advent of quality seismometers in the late 19th and early 20th centuries, our knowledge of Earth structure expanded rapidly with the discovery of the core by Richard Oldham in 1906, the crust-mantle discontinuity by Andrija Mohorovičić in 1909, and the inner core by Inge Lehmann in 1936. By 1939, Harold Jeffreys had produced a 1D global model of the whole Earth capable of matching P wave arrivals within 0.2% (see e.g. Lay and Wallace, 1995, ch. 1). In addition to the Earth, however, we have retrieved instrumental seismic data with clear evidence of interior signals only from the Earth's moon. The data from seismometers deployed on the Moon as part of Apollo Passive Seismic Experiment by astronauts in four of the six Apollo missions between 1969 and 1972, which recorded data until 1977, gave first order constraints on lunar structure, while also producing very unexpected seismograms showing high levels of scattering (e.g. Nakamura, 1983). While we have not received any more data from the Moon since the 1970's, recent research applying more more advanced seismological approaches developed since the initial studies have refined this model, and revealed more information about possible core layering and partial melting (Khan and Mosegaard, 2002; Lognonné et al., 2003; Chenet et al., 2006; Gagnepain-Beyneix et al., 2006; Khan et al., 2007; Garcia et al., 2011; Weber et al., 2011).

The power of seismology to illuminate planetary interiors is one of the primary motivations behind the planned InSight lander mission to Mars (Banerdt et al., 2013), which will include 3-component broadband and short period seismometers (SEIS experiment, (Lognonné et al., 2012a; Mimoun et al., 2012)), as well as a heat flow probe (HP^3), a geodetic experiment (RISE), and a magnetometer, in addition to meteorological sensors. While

2 seismometers, with sensitivity limited to 1 to 5 orders of magnitude lower than that of the Apollo seismometers, were landed on Mars during the Viking missions in the late 1970's, the seismometer on Viking 1 did not properly uncage, and the placement of the seismometer on the top of the Viking 2 lander prevented the recovery of any signals definitively originating in the planetary interior, although one possible internal signal was identified (Anderson et al., 1977). 20 years later, the second attempt with the OPTIMISM seismometers (Lognonné et al., 1998) onboard two Small Autonomous Stations (Linkin et al., 1998) was lost due to a Mars 96 mission launch stage failure. While the seismometer from the Viking mission did give us a solid upper bound on the Martian seismicity level and may have observed an internal event, the higher sensitivity of the InSight seismometer installation (both due to instrument sensitivity and installation on the surface of Mars rather than atop a lander), greatly enhances our capability of observing Martian seismicity. Despite the lack of seismic observational data to date, basic constraints from planetary mass and moment of inertia and some assumptions on bulk chemistry based on constraints primarily from SNC meteorites (McSween, 1994) have allowed for several estimates of the internal elastic and compositional structure of Mars (e.g. Mocquet et al., 1996; Sohl and Spohn, 1997; Gudkova and Zharkov, 2004; Rivoldini et al., 2011).

Many of the advances of Earth seismology have been built on the concept of networks of multiple instruments, which allow for accurate determination of source parameters for recorded quakes, and the four instruments of the Apollo Passive Seismic Experiment built on this legacy for planetary seismology. Logically, proposals for Martian seismometry, such as the NetLander mission (Lognonné et al., 2000; Dehant et al., 2004), have also attempted to set up networks using multiple landers. Multiple landers with geophysical instruments, however, lead to large expenses, and for this reason, the Insight mission has chosen to focus on a single lander and seismic station deployment, requiring a different strategy than simple body wave travel times inversion for the determination of the interior structure. While most of Earth seismology does rely on networks and the accurate locations they allow, there are many techniques that can be applied to single station data, including receiver functions (e.g. Phinney, 1964; Vinnik et al., 2001) and normal mode analysis (e.g. Lognonné et al., 1998). We focus on the ability of a single station approach like that of InSight to achieve the science goal of resolving mantle velocity structure within $\pm 5\%$, which will give us strong constraints on the internal structure and evolution of another terrestrial planet for the first

time. In this study, we verify the potential of single-station data using locations determined from multiple orbit surface waves both for determination of tectonically active regions as well as allowing for travel time inversions for 1D mantle velocity structure. Surface wave dispersion analysis is also possible with single station data, and we show that we should be able to resolve upper mantle velocity structure with group velocity dispersion measurements made at a single station using multiple orbit surface waves.

2. Expected Martian seismicity

Given the lack of direct observations of seismic activity from the Viking landers compared to the installation and instrument noise observed in that experiment (Anderson et al., 1977), we are able to constrain a rough upper bound on seismicity (based on the lack of observations) roughly equivalent to intraplate activity on Earth (Solomon et al., 1991). The Earth's intraplate activity level (the number of events per year of a given seismic moment) is shown by the solid red line on fig. 1. On the other hand, we would expect there to be a higher rate of cooling on Mars than on the Moon, and would therefore expect seismicity rates due to thermal contraction to be higher than lunar rates (e.g. Solomon et al., 1991; Phillips, 1991; Knapmeyer et al., 2006, see red line with triangles on fig. 1). Constraining the seismic activity of Mars, therefore, will obviously be a first order result from the proposed InSight mission.

Seismicity levels can also be estimated in advance of instrumental data by using thermal modeling (Phillips, 1991) or analysis of surface faulting (Golombek et al., 1992; Golombek, 2002; Knapmeyer et al., 2006) (fig. 1). While there is certainly a large amount of uncertainty in these estimates, most values cluster in a range which implies we potentially may observe 1-10 events with seismic moment near 10^{17} Nm (moment magnitude $M_W 5.3$) during the nominal Martian year duration of the mission. Excitation of normal modes above the observational limit (about 10^{-9} $\mathrm{ms}^{-2}/\mathrm{Hz}^{1/2}$) is likely for moment larger than 10^{17} Nm and will then allow inversions of the normal modes eigenfrequencies between 50 sec and 100 sec (Lognonné et al., 1996). We however do not discuss here such inversion, but instead focus on smaller quakes, expected to occur at a higher rate and therefore possibly still observable even in the case of a weaker than expected seismicity of Mars.

Events near the range of 10^{16} to 10^{17} Nm in moment release are important as they will likely be large enough to observe multiple orbit surface

waves (i.e. surface waves that either travel on the major arc to the station or have at least one full great-circle transit of the planet). When recorded on a quiet station on Earth, these multiple orbit surface waves begin to become reliably observable for events with a moment of $\sim 10^{18}$ Nm (M_W 6). These low amplitudes are mainly related to attenuation effects: Rayleigh surface waves at 100 sec have group velocity of about 3.8 km/s and a quality factor of Q = 120, so the attenuation factor (α_{Earth} =exp($-\frac{\omega t}{2Q}$)) after one circuit around the planet (about 3 hr) is about 1/15. Even if the mantle attenuation of Mars is relatively high (i.e. relatively low Q), the Martian thermal lithosphere (which on Earth has relatively low attenuation) is expected to be much thicker and the attenuation of such a surface wave, which has peak energy at a depth of 100-200 km, is therefore expected to be much less than on Earth (Lognonné and Mosser, 1993; Nimmo and Faul, 2013). The corresponding Martian attenuation factor is therefore expected to be

$$\alpha_{\text{Mars}} = \alpha_{\text{Earth}}^{\left[\frac{a_{\text{Mars}} \times Q_{\text{Earth}}}{a_{\text{Earth}} \times Q_{\text{Mars}}}\right]}, \tag{1}$$

where a_{Earth} and a_{Mars} are the radii of Earth and Mars, respectively. Both the smaller radius and the expected larger Q_{Mars} makes the attenuation factor much smaller on Mars. Even if we assume identical Q on Mars to Earth, multiple orbit surface waves will have amplitudes that are larger roughly by an order of magnitude simply due to the smaller planetary radius(fig. 2). The likely higher Q on Mars due to the expected thicker thermal lithosphere would only enhance this effect. For this reason, it is reasonable to expect that multiple orbit surface waves will likely be observable for events with moments ranging from 10^{16} Nm to 10^{17} Nm.

3. Surface wave-based single station location

In order to use surface waves for location, we need to be able to record multiple orbit surface waves. At a minimum, we need to be able to measure timing of the minor and major arc, plus the third orbit (minor arc plus another trip around the great circle path). We break the location problem into two parts. First, we determine distance and origin time from the timing of the first three orbits. This should be a relatively robust approach, as it relies only on the vertical component, which is likely to be the least noisy component of data recovered. This determination alone is sufficient for using body wave travel times to perform inversions for spherically averaged

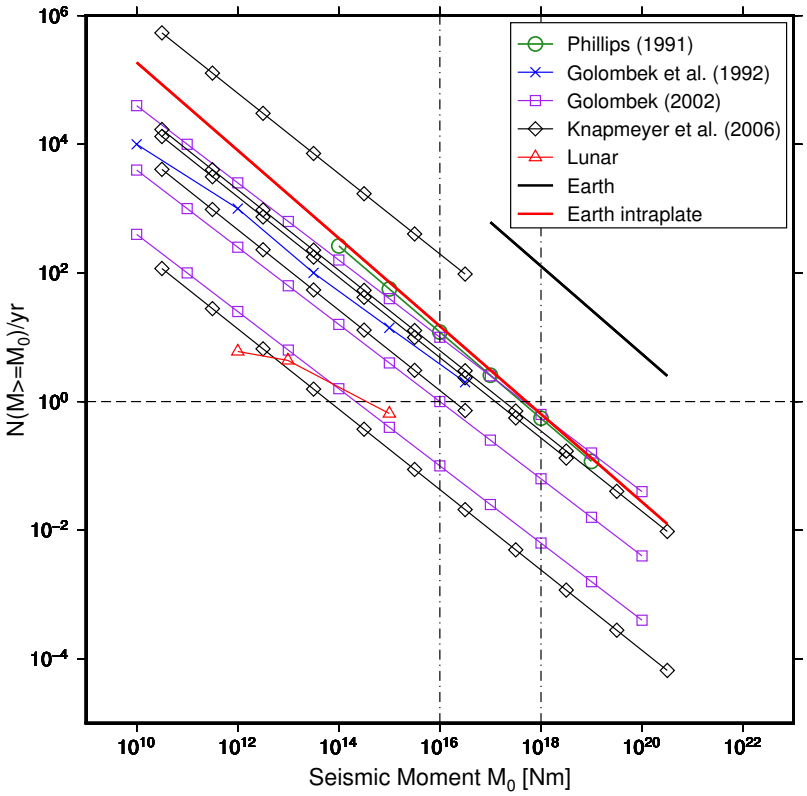

Figure 1: Estimates of Martian seismicity plotted as the number of events per Earth year greater than a given seismic moment vs. moment. Earth activity line is derived from a fit to the linear portion of the Harvard CMT catalog from 1984-2004 (Dziewonski and Woodhouse, 1983), while the intraplate line is simply 0.5% of the full Earth moment release based on studies of continental intraplate seismicity (Johnson and Kanter, 1990; Okal and Sweet, 2007). The lunar activity line is derived from the catalog of Nakamura et al. (1979). The dashed horizontal line represents the level above which we would expect to see a few events during the InSight mission, while the vertical dash-dot lines at 10^{16} and 10^{18} Nm represent the moment range over which we would expect 3rd orbit Rayleigh waves to become observable. Figure adapted from Knapmeyer et al. (2006).

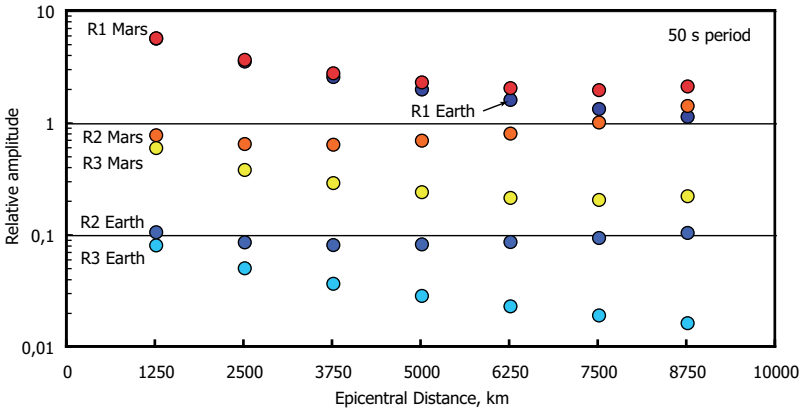

Figure 2: Amplitude of Rayleigh wave trains with a period of 50 s normalized by R1 (minor arc) amplitude at an epicentral distance of 10,000 km on Earth. Calculations are made assuming identical spatial Q of 150, and only taking into account differences in geometrical spreading and propagation distance. Note that R2 and R3 on Mars are larger than on Earth by roughly an order of magnitude.

structure. Next, we determine back azimuth using rotation of the horizontal components. Of course, this measurement may be more problematic with data from the single seismic station of the InSight mission, but we demonstrate that we can localize events within large tectonic regions if we do have horizontal measurements of sufficient quality.

3.1. Distance and origin time

If we are able to record up to 3rd orbit surface waves, determining distance and origin time of the source is a straightforward process. For this process, we filter the data in a series of frequency bands and take the envelope in order to pick the maximum energies of the first three orbits of the Rayleigh wave. Let us denote the arrival times at a given frequency band $R1$, $R2$, and $R3$. The angular group velocity is then

$$U = \frac{2\pi}{R3 - R1}, \tag{2}$$

where the angular distances are measured in radians, and angular group velocity is in radians/sec. These velocities can be converted to more typical units such as km/sec by multiplying by the planetary radius. The epicentral distance, Δ, and origin time, t_0, can then be derived as

$$\Delta = \pi - \frac{1}{2}U(R2 - R1) \tag{3}$$

$$t_0 \;=\; R1 - \frac{\Delta}{U}. \tag{4}$$

Of course, we could do a similar process for the Love waves, but noise is expected to be lower on the vertical component (based on both experience with terrestrial seismic deployments and expectation of pressure-induced tilt noise on the horizontal components in the surface wave frequency band), and this will be the most robust means of estimating distance and origin time.

In order to verify this basic approach, and to determine the level of error in location that can be expected with such a procedure, we collected data from 36 shallow events at a variety of epicentral distances in the magnitude range M6.0-M6.5 measured on the Global Seismic Network station BFO, located at the Black Forest Observatory in Germany (fig. 3). The event locations and CMT moment magnitudes (Ekström et al., 2012) are shown in table 1. Note that the initial data selection was based on a catalog of body wave (m_b) magnitudes, and so a few of the CMT M_W magnitudes are above and below the original range (ranging from 5.68 to 6.88 in M_W). The events discussed in this paper were chosen primarily to get a relatively even distribution of shallow events as a function of distance and then applying our processing approach to the first few events in each distance range for which we were able to visually identify R2 and R3 arrivals in 100 second lowpass filtered data. No further selection criteria were applied to the events to select "clean" data or advantageous focal mechanisms or to ensure azimuthal distribution. Note that we limit ourselves to shallow events because deep events do not excite fundamental mode surface waves efficiently. We filter the data with a series of zero phase Butterworth bandpass filters, and take the envelopes of the resulting seismograms (example shown in fig. 4). While R2 and R3 are typically not visually clear in the broadband time series data, these magnitudes are just large enough to allow the multiple orbit surface waves to emerge above the noise in some frequency bands, permitting us to assess how well such a method will perform if multiple orbit surface waves are observable for events recorded on Mars. We used an automated algorithm to select R1, R2, and R3 arrival times by picking peak energy values as a function of frequency. For each frequency band, we obtain an independent estimate of epicentral distance, Δ, and origin time, t_0, as well as group velocity, U as a function of frequency (which is used in section 5 to invert for upper mantle velocity structure). Using multiple frequency bands allows us to assess the consistency of the source parameter estimates and throw out inconsistent data.

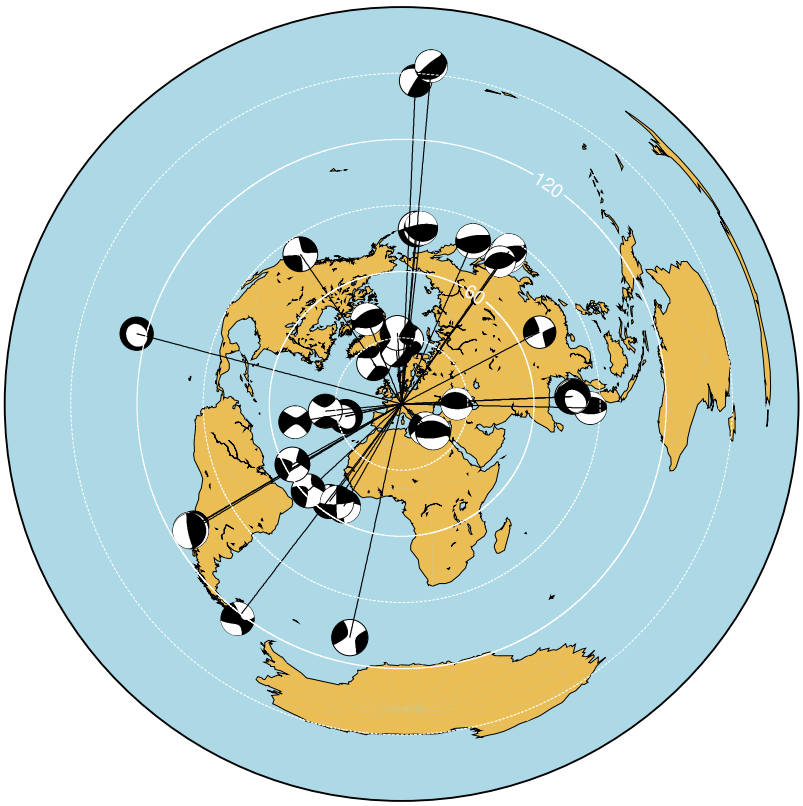

Figure 3: The 36 events used in this study plotted with their CMT focal mechanism (Ekström et al., 2012).

Event	Latitude	Longitude	Depth	Mw	Dist err (°)	t_0 err (s)
C200802201827A	36.24	21.73	17.6	6.16	-0.56	52.67
C200802210246A	77.02	19.28	12.8	6.07	0.64	24.81
C200805291546A	63.92	-21.17	12.0	6.29	-1.96	-61.53
C200907010930A	34.00	25.50	12.0	6.45	-0.59	-13.65
C200908200635A	72.22	0.84	12.0	5.99	0.21	11.09
C200909072241A	42.61	43.51	13.4	5.98	-3.07	16.43
C200704050356A	37.45	-24.44	12.0	6.34	0.06	0.56
C200704070709A	37.40	-24.38	12.0	6.06	-0.24	-11.54
C200903061050A	80.33	-2.32	13.0	6.47	-0.31	-7.35
C200906062033A	23.94	-46.12	12.0	6.00	-0.38	-9.61
C200907071911A	75.33	-72.49	16.5	6.03	-0.14	9.42
C200912091600A	-0.62	-20.80	26.5	6.41	-0.01	8.00
C201005251009A	35.31	-35.80	15.5	6.30	0.42	19.60
C200705041206A	-1.12	-14.92	12.7	6.22	0.29	-4.11
C200707030826A	0.81	-30.04	17.0	6.31	-0.34	1.55
C200707312255A	0.04	-17.86	21.8	6.17	-0.22	-10.59
C200708202242A	8.19	-39.17	12.0	6.54	0.63	5.95
C200803030931A	46.26	153.38	13.6	6.48	0.96	14.92
C200803151443A	2.47	94.51	12.0	6.03	-0.01	-28.15
C200804160554A	51.81	-179.17	12.0	6.60	-0.51	-5.83
C200805201353A	51.11	178.53	17.6	6.27	-0.34	9.45
C200805250821A	32.57	105.45	27.0	6.07	0.36	-66.22
C200806132343A	39.03	140.85	12.0	6.88	1.19	-17.84
C200806271140A	10.92	91.82	17.1	6.57	0.74	-11.66
C200806281254A	10.90	91.80	12.0	6.08	0.94	25.00
C201001100027A	40.53	-124.81	19.0	6.51	1.08	-5.05
C201003140808A	37.70	141.98	45.9	6.53	0.55	-65.16
C201003300102A	43.28	138.45	12.0	5.75	0.82	-23.56
C201001050455A	-58.50	-14.85	15.1	6.77	-1.26	-20.95
C201001171200A	-57.94	-66.16	18.6	6.24	0.33	65.24
C201002090103A	-15.00	-173.07	15.0	6.05	-0.02	19.95
C201002130234A	-22.19	-174.06	20.0	6.03	-0.30	-22.85
C201003070705A	-16.34	-115.45	12.7	6.26	0.29	7.10
C201003121650A	-34.41	-72.18	12.0	5.68	0.39	-20.28
C201003151108A	-35.96	-73.85	12.0	6.19	0.03	-39.27
C201003160221A	-36.49	-73.63	13.4	6.64	0.48	-14.94

Table 1: Event CMT identifiers, latitude and longitude (in degrees) and depth (km) for the dataset used in this study.

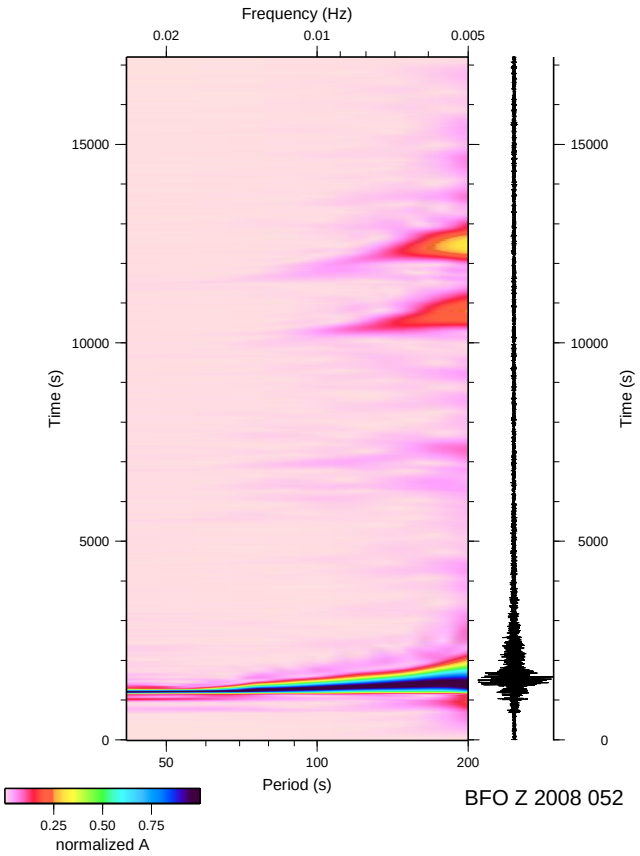

Figure 4: Example envelope processing for a magnitude 6.1 quake in Svalbard (event C200802210246A in table 1) at a distance of 29.1° from BFO. Color scale is normalized to peak amplitude in each frequency band. R2 can be seen at longer periods arriving between 10000 and 11000 s, and R3 between 12000 and 13000 s.

For our dataset of events recorded at BFO, we compared our estimated epicentral distances and origin times with the catalog locations to estimate the approximate error we can expect with such an approach on Martian data (fig. 5). As shown in the histograms and table 1, most events are located within 1° for epicentral distance (which corresponds to about 60 km on Mars) and 30 seconds in origin time, although a few outlying locations are included in the dataset. While these errors are clearly quite large in comparison with network-determined locations used in most terrestrial seismology applications, we are able to use them in combination with a small number of picked P and S arrival times (section 4) to invert for mantle velocity profiles that meet InSight mission requirements.

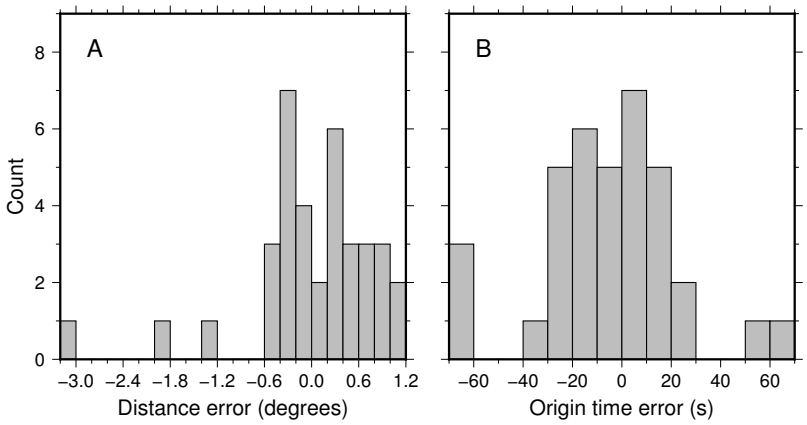

Figure 5: Histograms of errors in epicentral distance (A) and origin time (B) estimated from multiple orbit Rayleigh wave arrival times relative to catalog locations.

3.2. Back azimuth determination

While epicentral distance and origin time are adequate for the inversion of travel times for 1D velocity structure, we also need back azimuth in order to localize any recorded events to a particular tectonic region on Mars. While most event location schemes on the Earth rely on travel times recorded in a network of stations, it is possible to determine the back azimuth based on the polarization of particular seismic phases recorded on 3-component seismograms. For example, any P-SV phases will be polarized in the great-circle plane containing the source and receiver, and can be used to determine back-azimuth. For this study, we are focusing on the utility of the longer period surface wave data, and the known elliptical particle motion of Rayleigh

waves has been utilized in the past for single station location in the context of nuclear monitoring on Earth (e.g. Chael, 1997; Baker and Stevens, 2004). Any such polarization approach relies on high quality three component data with relatively low noise on on the vertical as well as horizontal components. The data used in this study, taken from BFO, comes from a station with consistently low noise on the horizontal components, but this is dependent on installation and site characteristics, and will likely be different for InSight data.

Using Rayleigh waveforms for back azimuth determination relies on the retrograde elliptical particle motion which is polarized in the great circle path between the source and receiver. When 3-component data is rotated into the source-receiver great-circle reference frame, the longitudinal component (along the great-circle path in the direction of positive minor arc propagation) is proportional to -1 times the Hilbert transform of the vertical component (e.g. Lay and Wallace, 1995). We can then determine the proper back azimuth (180° from the azimuth of the properly rotated longitudinal component) by rotating the horizontal components to determine the peak correlation with the Hilbert transformed vertical component in a time window containing minor arc Rayleigh wave energy. It is important to note that this technique does not have the 180° uncertainty of many body wave-based polarization approaches which rely on separation of P-SV and SH energy (see e.g. Frohlich and Pulliam, 1999). Such approaches may be very important tools for Mars data if we are attempting to determine back azimuth using body waves, particularly if we are not able to observe impulsive arrivals. Also, prograde elliptical particle motion has been modeled to occur on Earth in some frequency bands due to the presence of thick, very low velocity sedimentary basins (Tanimoto and Rivéra, 2005). The regolith on Mars may exhibit such properties, and so careful modeling and observation will be necessary to avoid 180° errors in our estimates. Such motion would likely be characterized by large horizontal motions relative to vertical motions in the Rayleigh wave (Tanimoto and Rivéra, 2005), and would likely exist only over a relatively narrow frequency band, so care must be taken to identify observations that may be affected by such particle motion.

In order to test how well we are able to determine back-azimuth in an installation with very low noise on the horizontal components like BFO with this approach, we take the data for each of the events we analyzed and filter it with a series of narrow band passes centered on periods from 50 to 190 seconds. Each frequency window is a 2 pole zero phase Butterworth filter with

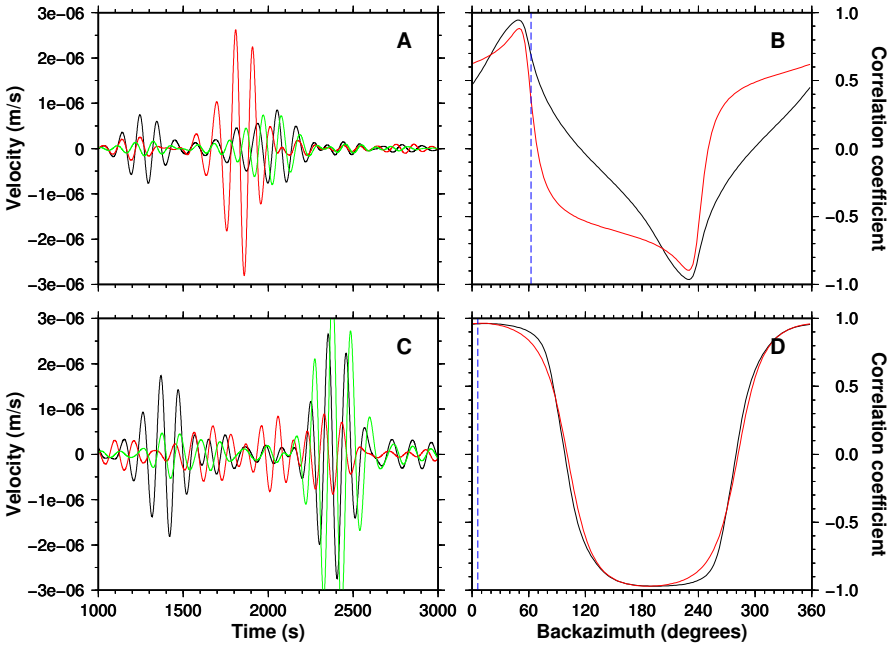

Figure 6: 3-component seismograms and correlation of rotated horizontal components to Hilbert transformed vertical component for two representative events at 70.8° (A and B) and 80.5° (C and D). Seismograms (A and C) show the vertical (green), longitudinal (black), and transverse components (red). The first packet of energy in both sets of seismograms is the S phase, while the second pack is the fundamental mode Love wave (on transverse component) and Rayleigh wave (on vertical and longitudinal). Panels B and D show correlation coefficient calculated in a time window centered on the Rayleigh wave arrival as a function of azimuth of rotated horizontal component averaged over calculations in several narrow frequency bands (black) or calculated on the broadband data (red). The back azimuth to the catalog location is shown with the blue dashed line.

corners at ±20% of the center period. In each frequency window, we rotate the horizontals through all azimuths with a 2° interval. For each rotation we calculate the correlation coefficient between the Hilbert-transformed vertical component waveform and the chosen horizontal azimuth in each frequency band. We then simply take the average of these correlation coefficients across all frequency bands at each azimuth and plot them to determine the maximum correlation (black lines in fig. 6B and D), which should correspond to the appropriate back azimuth. Alternatively, we can calculate a single correlation as a function of back azimuth on the broadband data including the whole passband between 50 and 190 seconds (red lines in fig. 6B and D).

The precision of the correlation peak depends strongly on the relative amplitude of the Love wave and Rayleigh wave energy in the correlation window. For an event with very strong Love wave energy (fig. 6A), the correlation curve is strongly peaked since a small misrotation will include significant Love wave energy. If there is little Love wave energy in the correlation window, though, the correlation peak is significantly broader and precision of back azimuth determination is lower (fig. 6C). Note that even in the case of a high-precision determination, there is still a mismatch between estimated back azimuth and the true back azimuth (dashed blue line in fig. 6B). This is likely due to 3D effects resulting in off-great circle propagation of the Rayleigh wave. Although Mars has very large topographic variations, surface waves are found to be much less sensitive to crustal variation than on Earth (Larmat et al., 2008), and we therefore expect these effects to be reduced on Mars. The correlation functions are generally more symmetric around the peak value when calculated as the average across several narrow frequency bands (black line in fig. 6B and D) than for that calculated on the broadband data (bandpass between 50 and 190 seconds, red line in fig. 6B and D). The asymmetry of this peak is a function of the phase relations between the Love and Rayleigh wave energy which vary strongly as a function of frequency. Averaging over several frequency bands tends to enhance symmetry, while the broadband data is more strongly dominated by the higher frequency energy and allows for significant asymmetry.

Once the back azimuth is determined, we combine that with the epicentral distances determined in section 3.1 to determine actual event location. We compare these estimated locations with the catalog locations for all events in our dataset (fig. S1 and S2 in supplementary material). We calculate location using back azimuths computed from the correlation function as determined by the average over narrow bands or using the broadband data (fig. 7). For

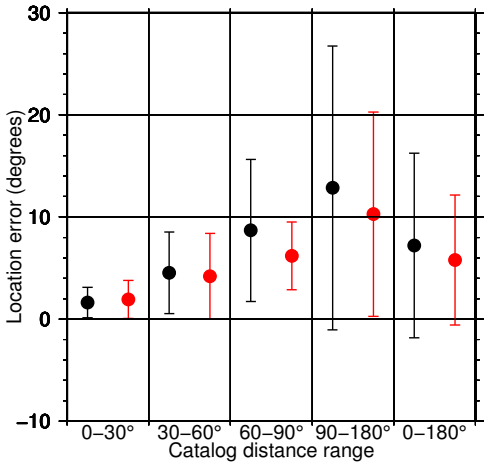

Figure 7: Average and standard deviation of errors of estimated locations relative to catalog locations. In each distance bin the errors are shown for locations calculated from averaging the back azimuth correlation function across many different narrow frequency bands (black) or for just calculating the correlation function on the broadband data bandpass between 50 and 190 seconds (red).

all but the closest events, the broadband determination of back azimuth gives marginally better locations. Across all events studied, the average error is less than 10 degrees, which should be adequate to associate a given event with a particular large tectonic region on Mars, although not enough to associate it with any mapped faults. The errors are largest for events near 90° in distance, due to the geometric effect that a given error in back azimuth leads to a maximum error in location at that distance. Events less than 30 degrees from the station, however, are generally located within 2 to 3 degrees of their catalog locations. Hypocentral depth is not determined in this inversion, and will likely be very difficult to determine with a single station due to depth and origin time tradeoffs, unless we are able to unambiguously identify depth phases. Once again, it is important to emphasize that polarization-based methods of back azimuth determination like this rely on high quality recordings for all 3 components, unlike the rest of this study which can be achieved with high quality measurements on the vertical component alone. This study with BFO data is a best case scenario, given the low noise on the horizontal components of BFO. If the actual installation on Mars has higher noise on the horizontal components, this portion of the location approach may only be possible for the largest events.

4. Body wave travel time inversion

If we have epicentral distance and origin time, and are able to identify body wave phase arrival times, we have enough information to perform body wave travel time inversions for one dimensional mantle velocity structure. For Earth data, events large enough to allow for the identification of multiple-orbit surface waves consistently produce easily identifiable body wave phases. In order to test how well an inversion can resolve structure using only a few body wave arrival times with the relatively large location and origin time errors of this simple, single-station approach, we picked P and S arrival times for the 28 events in our dataset at distances less than 90° from BFO (fig. 8). All P and S arrivals for the events analyzed were clear and impulsive. Fig. 8 shows clearly the additional scatter in these travel times introduced by the errors in epicentral distance and origin time from the surface wave determination as compared to the catalog locations. Of course, body wave travel times also depend on depth of the event. For the events in this dataset, all catalog depths are less than 50 km, and so the error from assuming a surface source for travel time calculations is small relative to the other errors in epicentral distance and origin time. Deep events may indeed occur on Mars (e.g. Solomon et al., 1991), but such events are unlikely to excite fundamental mode surface waves to a sufficient amplitude to allow for observation of multiple orbit surface waves, and so we can assume shallow sources for events located in this manner.

These travel times allow for an inversion for 1 dimensional crust and mantle velocity structure using very minimal *a priori* information. In a sense, we are simply attempting to apply the methods used in Earth seismology in the early 20th century. Ideally, if our velocity structure contains no low velocity layers, and our travel time picks are accurate enough, there is an analytical solution based on ray theory for the 1D structure known as the Herglotz-Wiechert equation (Herglotz, 1907; Wiechert, 1910; Lay and Wallace, 1995). Unfortunately, this approach depends strongly on the slope of the derived travel-time curves, and the large scatter of our travel time estimates does not allow for stable application of this approach. We instead perform a series of simple, iterative 1D inversions using ray theory and ray paths calculated with the TauP software package (Crotwell et al., 1999). The ray paths are calculated in an initial, assumed starting model, and are then used to calculate sensitivity for a damped least squares inversion for an improved velocity model in which the ray paths and predicted travel times are

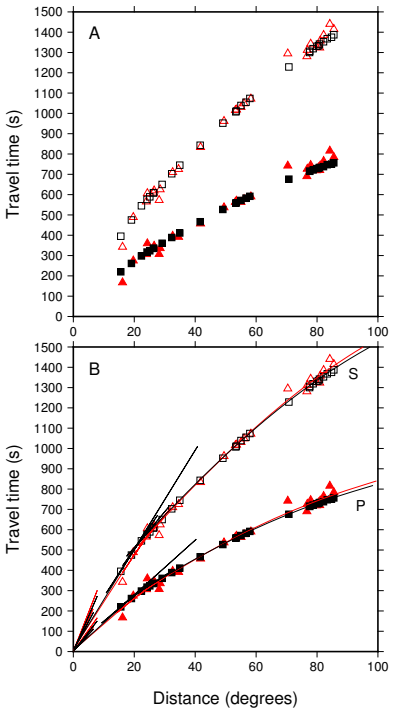

Figure 8: (A) Picked travel times for P (filled symbols) and S (open) relative to surface wave estimated origin time and epicentral distance (red) and catalog distance and origin time (black) for 28 events with distance less than 90°. (B) Picked travel times (as in A) compared with predicted travel times from PREM (black lines, Dziewonski and Anderson, 1981) and the model derived from the 28 P and S travel times with mineral physics-fixed gradients (red lines). The corresponding velocity model is shown in thick red lines in fig. 9B.

recalculated. The inversion is iterated until the travel time misfit converges. Our initial modeling approach simply assumes a crustal thickness of 40 km (thicker than most global reference models, but the sensitivity of the dataset to crustal properties is small), and then invert for a series of layers with piecewise continuous linear velocity structure with five 400 km thick layers down to 2040 km and an additional 1000 km thick layer down to 3040 km (thick red lines in fig. 9A). The models are constrained to non-negative velocity gradients. Low velocity layers certainly occur on the Earth, but they are difficult to resolve with sparse and noisy datasets, and allowing for negative gradients in the solution inhibits convergence of the iterative inversions. While this is a non-linear inverse approach, the resolved models are quite stable as a function of assumed starting model (fig. S3 in supplementary material). While the resolved model differs clearly from reference Earth models such as PREM (Dziewonski and Anderson, 1981), it reproduces the most general features of reference Earth models with a higher velocity gradient in the transition zone, but lower gradients in the uppermost and lower mantle. Additionally, the resolved models are within the 5% uncertainty range specified in the mission requirements of the InSight mission.

As we expect to only record less than 10 events large enough to obtain 3rd orbit Rayleigh waves and use this location approach, we further divide the dataset of 28 events into 4 independent subsets of 7 events that each roughly spans the distance range to 90°, and invert them using the same approach as the full dataset. As shown in the thin lines in fig. 9A, the resulting models show some scatter about the model resolved with the full dataset, particularly in the upper mantle as well as the velocity gradient in the lowest 1000 km of the model, consistent with the fact that we see the largest scatter in our particular set of travel time estimates at distances less than 30° and greater than 80°.

The initial modeling approach used very little *a priori* information about the 1D velocity structure, which may be appropriate for initial velocity structure estimates in a planetary single seismic station mission. However, we do have some constraints on the chemistry of the Mars, and we can use this to infer some constraints on mantle velocity structure, such as likely depths of phase transitions and approximate velocity gradients within given layers (e.g. Mocquet et al., 1996). For Mars, we have constraints about crustal chemistry from samples of the SNC meteorites, widely believed to be igneous rocks of Martian origin (McSween, 1994). Using a variety of assumptions, these can be used to model overall major element mantle chemistry (see

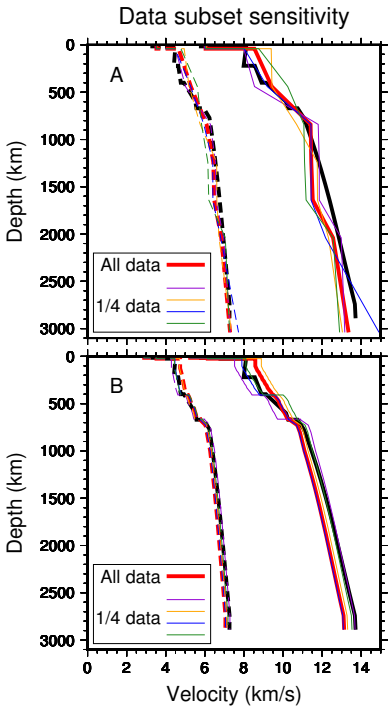

Figure 9: P (solid lines) and S (dashed lines) velocity models derived using P and S travel times and location and origin times derived from surface waves, compared with PREM (black lines). The models are parameterized with a single velocity crust, and either a series of piecewise linear velocity segments (A) or absolute perturbations to layers with velocity gradients fixed to that of a modified PREF (B). Models derived using all 28 events are shown with thick red lines, while models derived using 4 independent subsets of 7 events are shown with thin purple, orange, blue and green lines.

Lognonné and Johnson, 2007; Rivoldini et al., 2011, for a review of some of these models) . Given these estimates of bulk chemistry, estimates can be made of mineral abundances based on *ab initio* calculations and experimental phase diagrams for the pressure and temperature conditions modeled for the Martian interior (e.g. Verhoeven et al., 2005; Khan and Connolly, 2008; Rivoldini et al., 2011). For a given mineral assemblage, we can then use thermodynamic properties to extrapolate measured properties of those minerals to the appropriate pressure and temperature conditions, as has been done for several predicted models of Martian seismic structure (Mocquet et al., 1996; Sohl and Spohn, 1997; Gudkova and Zharkov, 2004). While uncertainties in the assumed bulk chemistry and other methodological approaches lead to differences between these models, and large differences in core radius and properties are allowed depending on assumed core state and composition, there is general agreement on the basic characteristics of the Martian mantle velocity structure in terms of approximate velocity gradient and location of phase-transition induced discontinuities. To simulate this level of *a priori* constraint with our Earth-based verification dataset, we choose to start our inversion with a mineral physics based model of 1D Earth velocity structure (PREF, Cammarano et al., 2005). There are actually a family of PREF models which are defined by predicting seismic velocities using a series of mineral physics parameters constrained by seismic data. We choose to start from a PREF-derived model here rather than a purely seismically derived 1D model such as PREM because we will not have a purely seismically defined model to start from on Mars, but we can make inferences based on mineral physics parameters. In this study, we then invert for a model with gradients fixed to that of a PREF-derived model, and simply invert for absolute velocity perturbations within a series of layers separated by major discontinuities in the model (the Moho, fixed at 24 km, the '410' which is at 408 km in PREF, and the '660', at 664 km in PREF). The actual starting model was derived from the PREF model distribution using one particular model choice (au-10845) with the high-velocity lid in the uppermost mantle removed in order to avoid any negative velocity gradients, which can lead to instabilities in the path calculations in the iterative travel time inversion. The PREF model is derived using large amounts of seismic data in combination with mineral physics constraints, and so of course provides a much better match to seismic data than we could ever expect of an *a priori* model of Martian velocity. We therefore start our inversions with the PREF model both increased and decreased by a factor of 10% (see fig. S4 in supplemen-

tary material). Note that this factor affects both the absolute velocities as well as the gradients of the models (similar to the uncertainty we expect in *a priori* Martian velocity models), and so leads to some differences in the final resolved models, particularly in the amplitude of the velocity jumps for the mantle discontinuities, which are not well constrained by this limited dataset. The overall velocity structure remains quite similar throughout the mantle. Inversions are performed both for the full dataset of P and S travel time picks as well as for the subsets of 7 events using the reduced velocity PREF as the starting model (fig. 9B). For the subsets, it is clear that the lower mantle structure is quite stable between the data subsets, while the uppermost mantle above the 410 km discontinuity shows more variability. In particular, the model derived using the data subset containing the closest event (C200802201827A in table 1, model shown by orange line in fig. 9A and B), which was mislocated by 0.56° too far and 52 seconds late on the origin time (fig. 8), is clearly biased to high upper mantle velocities in both the unconstrained and PREF-constrained inversions.

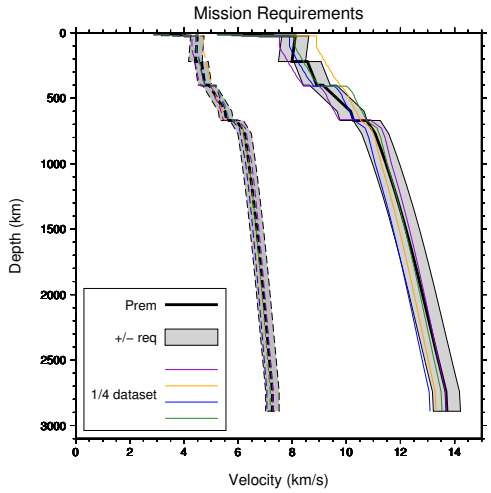

Figure 10: Comparison of the subset-derived models from fig. 9B (same colors and line properties for the subset models and PREM) with the mission requirements of InSight (± 250 m/s in V_S and 500 m/s in V_P) shown as thin black lines and grey box relative to the PREM mantle velocity.

Obviously, inversions of small datasets of 7 events with relatively large errors in epicentral distance and origin time lead to some variability in resolved velocity models. However, given this variability, we need to determine

whether we are able to resolve mantle velocity structure within the science requirements of the InSight mission. For this mission, we aim to resolve mantle S velocity structure within ±250 m/s and P velocity within ±500 m/s. For the Earth verification test here, we can compare the spread of the 7 events derived models with this level of uncertainty compared with PREM (fig. 10). As shown in the figure, all S velocity models fall closely within this range. For the P velocity models, there is a little more scatter in the upper mantle, primarily due to the nearest event, as discussed above. The lower mantle is in good agreement with the mission requirements in all models when the velocity gradients are constrained with mineral physics models, despite the scatter in arrival times at distances larger than 80°. Travel time inversions of small datasets of P and S wave picks relative to locations determined by multiple orbit surface waves do appear to be capable of resolving the mantle velocity structure, but it would be good to improve the upper mantle velocity models as well, as this dataset demonstrates that it can be biased by a relatively close event that is not well located. Fitting a travel time curve, like any curve fitting approach, is vulnerable to biases due to errors near the endpoints, which means that the largest errors might be expected in the shallowest and deepest mantle. Of course, if we have enough events which can be located, we can iteratively improve the model as more data becomes available, but there may be only a few events recorded of sufficient magnitude. Fortunately, the great-circle averaged group velocity information derived from our location algorithm can also help constrain the uppermost structure to help avoid these biases for the shallow structure.

5. Inversion of group velocity dispersion diagrams

Given observations of first and third orbit Rayleigh waves, we can obtain group velocity dispersion diagrams (e.g. fig. 11d-f). Probabilistic estimations of Rayleigh wave group velocity are preferred to single deterministic dispersion curves since R3 is not easily pickable, due to the dispersion of surface waves. Probability distributions are obtained by combining a single pick for R1 wave train for each frequency, which is relatively impulsive with any narrow band filter, and a exploration of all group velocity values to test the third orbit arrivals. For a given frequency and group velocity, an R1 pick is made by automatic maxima detection, and a trial amplitude value for R3 can be extracted from the signal envelope using eq. 2. The product of the amplitudes of R1 and R3 can therefore be seen as the likelihood for R3

arrival time for that combination of frequency and group velocity. After normalization and windowing, this weight is turned into a misfit value plotted using greyscale as in fig. 11d-f. This plot can then be converted to a probability distribution function, showing the degree of reliability of the group velocity value for each frequency. In practice, group velocities are bounded between 3 and 5.5 km/s over these frequencies, which allows for a wide range of possibilities. Note that these dispersion diagrams are independent of the location determined in the previous sections. They rely only on the full great-circle propagation difference between R1 and R3. This dispersion data may be used to directly retrieve the 1-D V_S profile of the upper mantle averaged along the great circle. The originality of the approach described in this study is that the non-linearity between the data and the parameters is fully taken into account thanks to a Bayesian method. First, synthetic data are tested, using two different models of the Martian mantle. Second, group velocities computed from event C200802210246A (table 1) recorded at BFO are considered. The results demonstrate the potential of the data to achieve the $\pm 5\%$ requirement on V_S.

5.1. Inverse Problem

Bayesian approaches allow us to go beyond the classical computation of the unique best-fitting V_S model, in that they provide a quantitative measure of the model uncertainty and non-uniqueness (e.g. Mosegaard and Tarantola, 1995). While these methods are popular in geophysics, their use in global seismology is recent because of the large computational demand involved and the large amount of inverted parameters (e.g. Shapiro and Ritzwoller, 2002; Khan et al., 2009, 2013; Bodin et al., 2012; Mosca et al., 2012; Drilleau et al., 2013; Shen et al., 2013a,b). Our inverse problem consists of computing the V_S profile from surface wave dispersion diagrams. The data $\mathbf{d}$ are linked to the parameters $\mathbf{p}$ through the equation, $\mathbf{d} = A(\mathbf{p})$, where the non-analytic and non-linear operator A represents the forward problem. In the Bayesian framework, the solutions of the inverse problem are given by the posterior probability $P(\mathbf{p}|\mathbf{d})$ that the parameters are in a configuration $\mathbf{p}$ given the data are in a configuration $\mathbf{d}$. The parameter space is sampled according to $P(\mathbf{p}|\mathbf{d})$. Bayes' theorem links the prior distribution $P(\mathbf{p})$ and the posterior distribution $P(\mathbf{p}|\mathbf{d})$,

$$P(\mathbf{p}|\mathbf{d}) = \frac{P(\mathbf{d}|\mathbf{p})P(\mathbf{p})}{\sum\limits_{\mathbf{p}\in\mathcal{M}} P(\mathbf{d}|\mathbf{p})P(\mathbf{p})}, \tag{5}$$

where $\mathcal{M}$ denotes all the configurations in the parameter space. The probability distribution $P(\mathbf{d}|\mathbf{p})$ is a function of the misfit, which determines the difference between the observed data $\mathbf{d}$ and the computed synthetic data $A(\mathbf{p})$. To estimate the posterior distribution (eq. 5), we employ the Metropolis algorithm (e.g. Metropolis et al., 1953; Hastings, 1970), which samples the model space with a sampling density proportional to the unknown posterior probability density function (pdf). This algorithm relies on a randomized decision rule which accepts or rejects the proposed model according to its fit to the data and the prior.

The shape of the solution, the *a posteriori* pdf, is directly dependent of the misfit function and of the data uncertainties. A classical procedure is to take the maximum value of the energy diagram for each frequency as the dispersion curve measurement and to compute the associated standard deviation. The misfit function is then evaluated with a L_1 or L_2 norm. But this procedure is reductive because the dispersion diagrams obtained with real data give several maxima for a given frequency (see fig. 11f, for example). This non-linear behavior is taken into account thanks to the values of the dispersion diagram, which can be seen as the uncertainties on group velocities. In practice, each time a new model is randomly sampled, a score is given between 0 and 1 (here called 'misfit coefficient') for each frequency according to the position of the computed group velocity in the dispersion diagram. The sum of the scores for all the frequency gives the misfit value.

5.2. Computational aspects

We employ the probabilistic procedure developed by Drilleau et al. (2013), which relies on a Markov chain Monte Carlo algorithm. In what follows we give a very brief outline of the practical implementation of the method, and the reader is referred to Drilleau et al. (2013) for further details.

V_S profiles are described using C^1 Bézier curves (Bézier, 1966, 1967), based on randomly chosen control points (or Bézier points). The advantages of such a parameterization are that few parameters are required and that it does not need a regularly spaced discretization of the points in depth. This parameterization can thus be used to describe both smoothly varying models and first-order discontinuities. The inverted parameters are the vectors corresponding to the Bézier points for shear velocity values and the depths at which these points are located. Different amounts of control points are used to allow different degrees of complexity. From 1500 km depth to the center of the planet, the shear velocities are those of PREM (Dziewonski

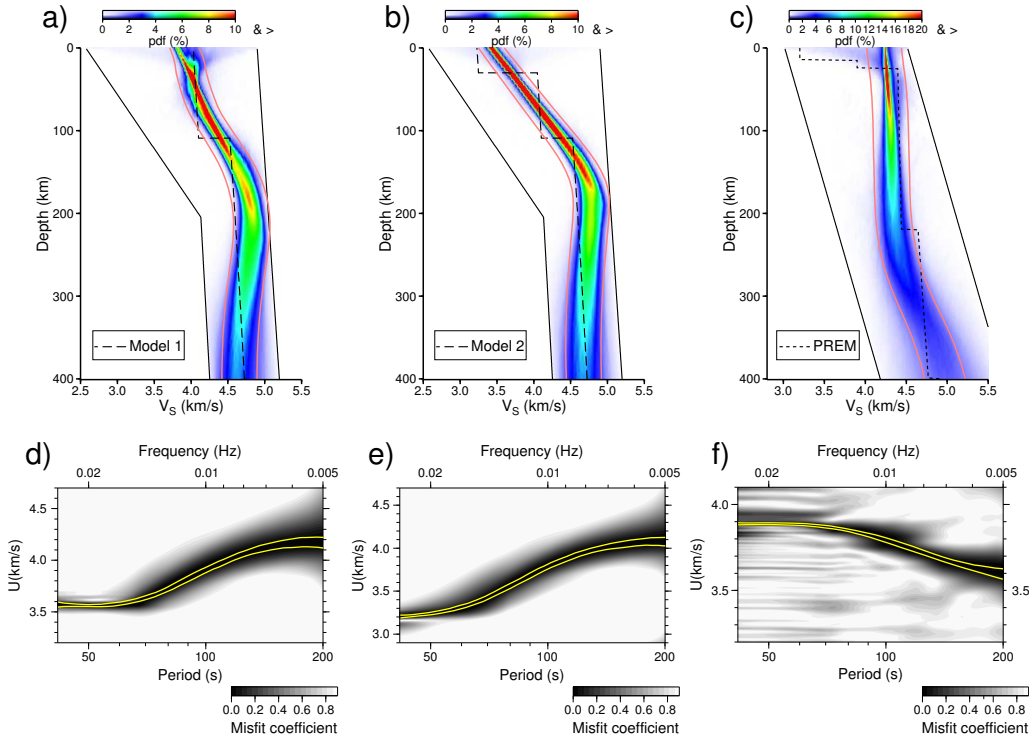

Figure 11: *A posteriori* probability density functions (pdf) of shear wave velocity (top) and input dispersion diagrams (bottom) for Model 1 (left), Model 2 (middle) and real data (right). In panels a–c, red and blue colors show high and low probabilities, respectively. Continuous black curves represent the minimum and maximum parameter values allowed. In total, 120,000 models were sampled. Pink curves delimit the interval between ±5% of the median V_S profile of the distribution. In panels d–f, the gray scale shows the weight assigned to each frequency and group velocity intervals when computing the misfit function. Yellow curves circumscribe the predicted group velocity values of all the models accepted by the Bayesian algorithm.

and Anderson, 1981) for the Earth and those of Sohl and Spohn (1997) for Mars. Considering the aforementioned boundary condition, the model contains between 18 and 26 parameters, depending on the number of Bézier points employed (between 11 and 15).

The Bayesian formulation enables to account for a priori knowledge. In this section we choose minimal prior information, which consists of uniform probability distribution in wide realistic parameter spaces. The V_S parameters are randomly sampled between the black curves in fig. 11a–c, which are the bounds of the model space. These bounds are chosen to sample the models between $\pm 10\%$ at least of the PREM or the Model A of Sohl and Spohn (1997). The reference seismic model only constrains the parameter range and its choice is not as crucial as in linearized inversions.

We use scaling relations based on the experimental study of Isaak (1992) to compute V_P and ρ profiles from V_S values. The attenuation profile used is PREM for the Earth. For Mars, the seismic attenuation proposed by Lognonné and Mosser (1993) after the observation of Phobos secular acceleration is used. Models are considered to be isotropic. The forward problem, which involves the computation of the fundamental mode of Rayleigh wave dispersion curves as a function of period (here chosen between 40 and 200 seconds period), is performed with the MINEOS package based on the work of Gilbert and Dziewoński (1975) and Woodhouse (1988).

5.3. Model and results

We apply this Bayesian inversion technique to both synthetic Martian and real terrestrial data. The present knowledge of the Martian crust thickness is still poor (see reviews by Neumann et al., 2004; Wieczorek and Zuber, 2004; Sohl et al., 2005; Sohl and Schubert, 2007; Mocquet et al., 2011), but all studies converge to extreme bound values in the range 30 - 100 km (e.g. Zuber et al., 2000; Nimmo and Stevenson, 2001; Nimmo, 2002). Here, two synthetic models of Mars with a thick crust are chosen. Model 1 is the velocity Model A of Sohl and Spohn (1997), with a 110 km-thick crust (dashed lines in fig. 11a). Model 2 has an additional layer mimicking an upper crust (dashed lines in fig. 11b). Real terrestrial data are also tested (fig. 11c and f).

The results of the Bayesian inversions are shown in fig. 11. Given that only the fundamental mode is considered, the surface wave sensitivity rapidly decreases below 400 km depth and the V_S distributions are not shown deeper. The V_S profiles are particularly well defined between the surface and 200 km depth, where the pdfs are the highest. For identical ranges of investigated

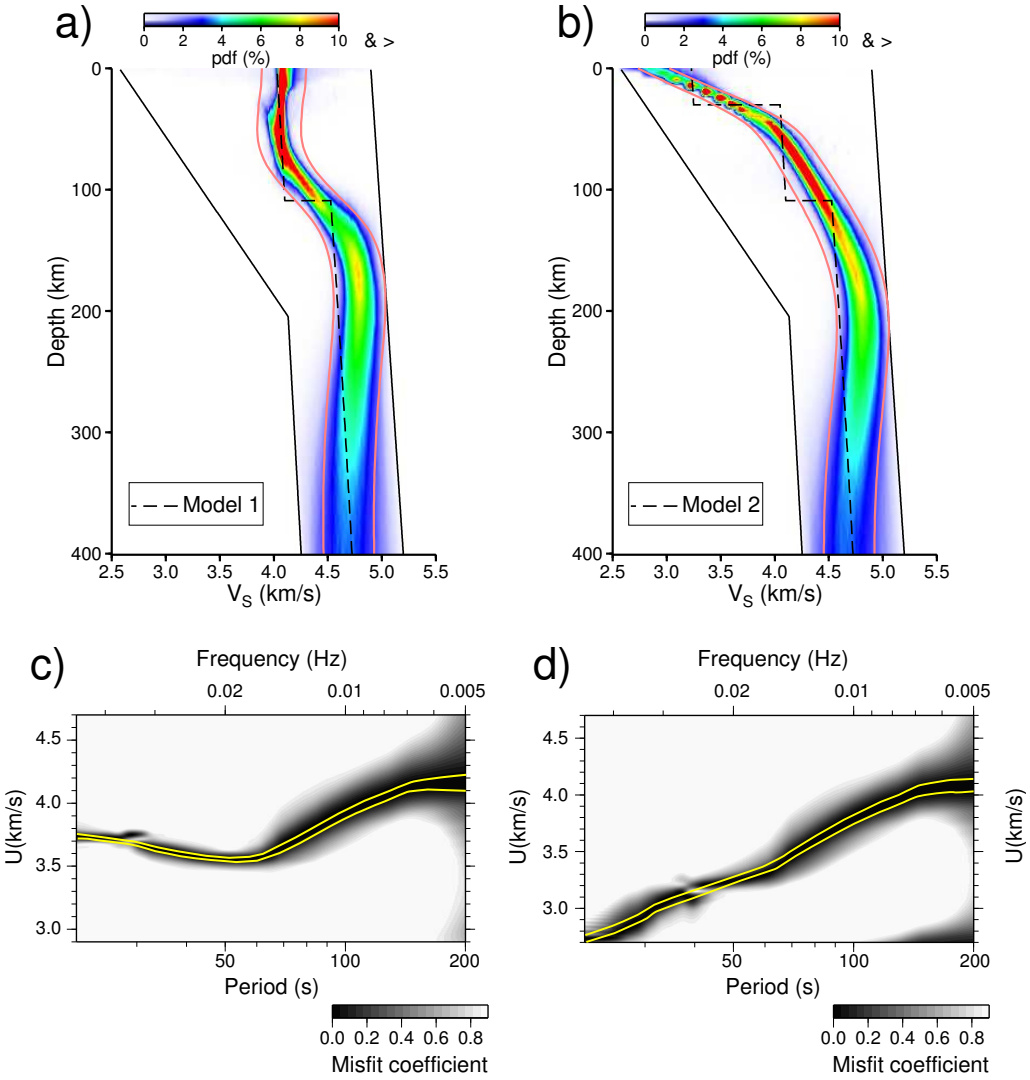

Figure 12: Results for Bayesian inversion of synthetic energy diagrams calculated down to 20 s period for Models 1 and 2, as in fig. 11. Color scale in panels a and b, and grey scale in d and e are defined as in fig. 11.

periods, the depth of well resolved seismic structures within the Earth and Mars extends to about 200 km, and 400 km, respectively, as expected from Mars' radius, about half the Earth's. Fig. 11a and b show that the distributions of Bézier curves are in very good agreement with the expected profiles. An important result is that for the synthetic data (fig. 11a and b), the ±5% intervals around the median profiles of the distributions contain the input models, which is one of the requirements of the InSight mission. For real data (fig. 11c), V_S values are globally lower than the PREM ones but the PREM is included in the ±5% interval.

The contours of the dispersion curves associated with the whole set of accepted models are plotted with yellow curves on the input dispersion diagrams (fig. 11d–f). They all match with the area of low misfit coefficients, which means that a large range of possible models could produce such a dispersion diagram. This good agreement between synthetic and tested data clearly supports the method employed here for elucidating the seismic structure of planetary mantles from a large number of models.

The terrestrial group velocity is not tightly constrained at periods shorter than ∼60 seconds for the studied event (fig. 11f), and therefore does not resolve crustal velocities (fig. 11c). Given a similar frequency range, the Martian synthetic tests do differentiate between the two different end member crustal models (Models 1 and 2), but the crustal structure is still greatly smoothed, particularly across the mid-crustal discontinuity in Model 2. While getting reliable dispersion data to higher frequencies may be problematic with great-circle average approaches, it may be possible using smaller events located using other location approaches that become feasible as the average mantle velocity is constrained by the large events located using the approach of this study. Synthetic tests with group velocity dispersion extended to 20 seconds allow us to determine more details about Martian crustal structure when such data is available (fig. 12).

6. Discussion

This study is not intended to robustly constrain the location capabilities and uncertainties of the particular InSight instrument installation on the surface of Mars. That will, of course, depend on the still undetermined noise characteristics of Mars and the installation itself, as well as the unknown seismicity level of Mars. Based on modeling of Viking wind data, the microseismic noise on Mars with periods between 1 and 100 seconds is expected

to be less than that on Earth by roughly an order of magnitude (Lognonné and Mosser, 1993), and this is supported by more recent numerical calculations based on large eddy simulations (Lognonné et al., 2012b). This study, however, is focused on demonstrating the effectiveness of an approach of determining locations and inverting for interior structure based on multiple orbit surface wave recordings if the seismicity level of Mars and noise levels of the InSight installation permit observations of such surface waves.

Further work is clearly necessary to work on enhancing techniques for observations of multiple orbit surface waves with lower signal to noise ratios in order to expand the range of this approach to lower event magnitudes and/or higher installation noise levels. Undoubtedly, other techniques using body waves will be necessary to locate smaller nearby events, and it is important to work on making such locations more robust when the initial velocity model is not well constrained, as will be the case in our initial observations on Mars.

7. Conclusions

Given the high quality design of the InSight experiment and current estimates of Martian seismicity, we have a high capability of detecting multiple orbit surface waves on Mars. Our study verifies that we can use such data recorded on a single station for events just above the threshold for observability of such signals. This data allows for location within $\sim 1^\circ$ in epicentral distance and 30 seconds in origin time, which is adequate to allow for recovery of mantle velocity structure within $\pm 5\%$ using inversion of P and S travel times for datasets with as few as 7 events. If we are able to record signals on the horizontal components with sufficient signal to noise ratio, backazimuth determination allows for absolute locations within 10°, which can localize the seismic source within a tectonic region of the Martian surface. Finally, the multiple orbit surface waves allow for the determination of fundamental mode group velocity dispersion independent of location error, which can more tightly resolve upper mantle velocities. Overall, such a single station dataset should allow us to get relatively tight constraints on the interior structure of Mars, giving us unprecedented constraints on the structure and evolution of another terrestrial planet.

Acknowledgements

This work was undertaken during the preparation phase of the SEIS experiment on InSight mission. MP was supported by funds from NASA/JPL

as part of the InSight mission, and EB, MD, AM, and PL acknowledge the financial support of CNES. The Bayesian inversions of group velocity dispersion diagrams were performed using HPC resources of CINES (Centre Informatique National de lEnseignement Suprieur) under the allocation 2014047062 made by GENCI (Grand Equipement National de Calcul Intensif).

References

Anderson, D., Miller, W., Latham, G., Nakamura, Y., Toksöz, M., 1977. Seismology on Mars. J. Geophys. Res. 82, 4524–4546.

Baker, G., Stevens, J., 2004. Backazimuth estimation reliability using surface wave polarization. Geophys. Res. Lett. 31, L09611. doi:10.1029/2004GL019510.

Banerdt, W., Smrekar, S., Lognonné, P., Spohn, T., Asmar, S., Banfield, D., Boschi, L., Christensen, U., Dehant, V., Folkner, W., Giardini, D., Goetze, W., Golombek, M., Grott, M., Hudson, T., Johnson, C., Kargl, G., Kobayashi, N., Maki, J., Mimoun, D., Mocquet, A., Morgan, P., Panning, M., Pike, W., Tromp, J., van Zoest, T., Weber, R., Wieczorek, M., Garcia, R., Hurst, K., 2013. InSight: A Discovery mission to explore the interior of Mars, in: 44th Lunar and Planetary Science Conference, Lunar and Planetary Inst., Houston, TX. p. Abstract #1915.

Bézier, P., 1966. Définition numérique des courbes et surfaces I. Automatisme 11, 625–632.

Bézier, P., 1967. Définition numérique des courbes et surfaces II. Automatisme 12, 17–21.

Bodin, T., Sambridge, M., Tkalčić, H., Arroucau, P., Gallagher, K., Rawlinson, N., 2012. Transdimensional inversion of receiver functions and surface wave dispersion. J. Geophys. Res. 117, B02301. doi:10.1029/2011JB008560.

Cammarano, F., Deuss, A., Goes, S., Giardini, D., 2005. One-dimensional physical reference models for the upper mantle and transition zone: combining seismic and mineral physics constraints. J. Geophys. Res. 110, B01306. doi:10.1029/2004JB003272.

Chael, E., 1997. An automated Rayleigh-wave detection algorithm. Bull. Seism. Soc. Amer. 87, 157–163.

Chenet, H., Lognonné, P., Wieczorek, M., Mizutani, H., 2006. Lateral variations of lunar crustal thickness from the apollo seismic data set. Earth Planet. Sci. Lett. 243, 1–14.

Crotwell, H., Owens, T., Ritsema, J., 1999. The TauP toolkit: Flexible seismic travel-time and ray-path utilities. Seis. Res. Lett. 70, 154–160.

Dehant, V., Lognonné, P., Sotin, C., 2004. Netlander: a European mission to study the planet Mars. Planet. Space Sci. 52, 977–985.

Drilleau, M., Beucler, E., Mocquet, A., Verhoeven, O., Moebs, G., Burgos, G., Montagner, J.P., Vacher, P., 2013. A Bayesian approach to infer radial models of temperature and anisotropy in the transition zone from surface wave dispersion curves. Geophys. J. Int. 195, 1165–1183.

Dziewonski, A., Anderson, D., 1981. Preliminary Reference Earth Model. Phys. Earth Planet. Inter. 25, 297–356.

Dziewonski, A., Woodhouse, J., 1983. An experiment in systematic study of global seismicity: Centroid-moment tensor solutions for 201 moderate and large earthquakes of 1981. J. Geophys. Res. 88, 3247–3271.

Ekström, G., Nettles, M., Dziewonski, A., 2012. The global CMT project 2004-2010: Centroid-moment tensors for 13,017 earthquakes. Phys. Earth Planet. Inter. 200–201, 1–9.

Frohlich, C., Pulliam, J., 1999. Single-station location of seismic events: a review and a plea for more research. Phys. Earth Planet. Inter. 113, 277–291.

Gagnepain-Beyneix, J., Lognonné, P., Chenet, H., Lombardi, D., Spohn, T., 2006. A seismic model of the lunar mantle and constraints on temperature and mineralogy. Phys. Earth Planet. Inter. 159, 140–166.

Garcia, R., Gagnepain-Beyneix, J., Chevrot, S., Lognonné, P., 2011. Very preliminary reference Moon model. Phys. Earth Planet. Inter. 188, 96–113.

Gilbert, F., Dziewoński, A., 1975. An application of normal mode theory to the retrieval of structural parameters and source mechanisms from seismic spectra. Philos. Trans. R. Soc. London A 278, 187–269.

Golombek, M., 2002. A revision of Mars seismicity from surface faulting, in: 33rd Lunar and Planetary Science Conference, Lunar and Planetary Inst., Houston, TX. p. Abstract #1244.

Golombek, M., Banerdt, W., Tanaka, K., Tralli, D., 1992. A prediction of Mars seismicity from surface faulting. Science 258, 979–981.

Gudkova, T., Zharkov, V., 2004. Mars: interior sturcture and excitation of free oscillations. Phys. Earth Planet. Inter. 142, 1–22.

Hastings, W., 1970. Monte Carlo sampling methods using Markov chains and their applications. Biometrika 57, 97–109.

Herglotz, G., 1907. Über das benndorfsche Problem der Fortpflanzungsgeschwindigkeit der Erdbebenstrahlen. Zeitschrift für Geophysik 8, 145–147.

Isaak, D., 1992. High-temperature elasticity of iron-bearing olivines. J. Geophys. Res. 97, 1871–1885.

Johnson, A., Kanter, L., 1990. Earthquakes in stable continental crust. Sci. Am. 262, 68–75.

Khan, A., Boschi, L., Connolly, A., 2009. On mantle chemical and thermal heterogeneities and anisotropy as mapped by inversion of global surface wave data. J. Geophys. Res. 114, B09305. doi:10.1029/2009JB006399.

Khan, A., Connolly, J., 2008. Constraining the composition and thermal state of Mars from inversion of geophysical data. J. Geophys. Res. 113, E07003. doi:10.1029/2007JE002996.

Khan, A., Connolly, J., Maclennan, J., Mosegaard, K., 2007. Joint inversion of seismic and gravity data for lunar composition and thermal state. Geophys. J. Int. 168, 243–258.

Khan, A., Mosegaard, K., 2002. An inquiry into the lunar interior: A nonlinear inversion of the Apollo lunar seismic data. J. Geophys. Res. 107, 5036. doi:10.1029/2001JE001658.

Khan, A., Zunino, A., Deschamps, F., 2013. Upper mantle compositional variations and discontinuity topography imaged beneath Australia from bayesian inversion of surface-wave phase velocities and thermochemical modeling. J. Geophys. Res. 116. doi:10.1002/jgrb.50304.

Knapmeyer, M., Oberst, J., Hauber, E., Wählisch, M., Deuchler, C., Wagner, R., 2006. Working models for spatial distribution and level of Mars' seismicity. J. Geophys. Res. 111, E11006. doi:10.1029/2006JE002708.

Larmat, C., Montagner, J.P., Capdeville, Y., Banerdt, W., Lognonné, P., Vilotte, J.P., 2008. Numerical assessment of the effects of topography and crustal thickness on Martian seismograms using a coupled modal solution–spectral element method. Icarus 196, 78–89.

Lay, T., Wallace, T., 1995. Modern Global Seismology. Academic Press.

Linkin, V., Harri, A.M., Lipatov, A., Belostotskaja, K., Derbunovich, B., Ekonomov, A., Khloustova, L., Kremnev, R., Makarov, V., Martinov, B., Nenarokov, D., Prostov, M., Pustovalov, A., Shustko, G., Järvinen, I., Kivilinna, H., Korpela, S., Kumpulainen, K., Lehto, A., Pellinen, R., Pirjola, R., Riihelä, P., Salminen, A., Schmidt, W., Siili, T., Blamont, J., Carpentier, T., Debus, A., Hua, C.T., Karczewski, J.F., Laplace, H., Levacher, P., Lognonné, P., Malique, C., Menvielle, M., Mouli, G., Pommereau, J.P., Quotb, K., Runavot, J., Vienne, D., Grunthaner, F., Kuhnke, F., Musmann, G., Rieder, R., Wänke, H., Economou, T., Herring, M., Lane, A., McKay, C.P., 1998. A sophisticated lander for scientific exploration of Mars: scientific objectives and implementation of the Mars-96 Small Station. Planet. Space Sci. 46, 717–737. doi:10.1016/S0032-0633(98)00008-7.

Lognonné, P., Banerdt, W.B., Hurst, K., Mimoun, D., Garcia, R., Lefeuvre, M., Gagnepain-Beyneix, J., Wieczorek, M., Mocquet, A., Panning, M., Beucler, E., Deraucourt, S., Giardini, D., Boschi, L., Christensen, U., Goetz, W., Pike, T., Johnson, C., Weber, R., Larmat, K., Kobayashi, N., Tromp, J., 2012a. Insight and Single-Station Broadband Seismology: From Signal and Noise to Interior Structure Determination, in: Lunar and Planetary Institute Science Conference Abstracts, p. 1983.

Lognonné, P., Beyneix, J.G., Banerdt, W.B., Cacho, S., Karczewski, J.F., Morand, M., 1996. Ultra broad band seismology on InterMarsNet. Planet. Space Sci. 44, 1237. doi:10.1016/S0032-0633(96)00083-9.

Lognonné, P., Clévédé, E., Kanamori, H., 1998. Computation of seismograms and atmospheric oscillations by normal-mode summation for a spherical earth model with realistic atmosphere. Geophys. J. Int. 135, 388–406.

Lognonné, P., Gagnepain-Beyneix, J., Banerdt, W., Chenet, H., 2003. A new seismic model of the Moon: implication in terms of structure, formation, and evolution. Earth Planet. Sci. Lett. 211, 27–44.

Lognonné, P., Giardini, D., Banerdt, W., Gagnepain-Beyneix, J., Mocquet, A., Spohn, T., Karczewski, J., Schibler, P., Cacho, S., Pike, W., Cavoit, C., Desautez, A., Favède, M., Gabsi, T., Simoulin, L., Striebig, N., Campillo, M., Deschamp, A., Hinderer, J., Lévéque, J., Montagner, J.P., Rivéra, L., Benz, W., Breuer, D., Defraigne, P., Dehant, V., Fujimura, A., Mizutani, H., Oberst, J., 2000. The NetLander very broad band seismometer. Planet. Space Sci. 48, 1289–1302.

Lognonné, P., Johnson, C., 2007. Planetary seismology, in: Schubert, G. (Ed.), Treatise on Geophysics. Elsevier, Amsterdam. volume 10, pp. 69–122.

Lognonné, P., Mosser, B., 1993. Planetary seismology. Surveys Geophys. 14, 239–302.

Lognonné, P., Spiga, A., Hurst, K., Gabsi, T., Banfield, D., de Raucort, S., Mimoun, D., Banerdt, W., Hecht, M., 2012b. Atmospheric induced microseismic noise generation: Large eddy simulations, in: Lunar and Planetary Institute Science Conference Abstracts, p. 1994.

McSween, H., 1994. What we have learned about Mars from SNC meteorites. Meteoritics 29, 757–779.

Metropolis, N., Rosenbluth, A., Rosenbluth, M., Teller, A., Teller, E., 1953. Equation of state calculations by fast computing machines. J. Chem. Phys. 21, 1087–1091.

Mimoun, D., Lognonné, P., Banerdt, W.B., Hurst, K., Deraucourt, S., Gagnepain-Beyneix, J., Pike, T., Calcutt, S., Bierwirth, M., Roll, R., Zweifel, P., Mance, D., Robert, O., Nébut, T., Tillier, S., Laudet, P., Kerjean, L., Perez, R., Giardini, D., Christenssen, U., Garcia, R., 2012. The InSight SEIS Experiment, in: Lunar and Planetary Institute Science Conference Abstracts, p. 1493.

Mocquet, A., Rosenblatt, P., Dehant, V., Verhoeven, O., 2011. The deep interior of Venus, Mars, and the Earth: A brief review and the need for planetary surface-based measurements. Planet. Space Sci. 59, 1048–1061. doi:10.1016/j.pss.2010.02.002.

Mocquet, A., Vacher, P., Grasset, O., Sotin, C., 1996. Theoretical seismic models of Mars: the importance of the iron content of the mantle. Planet. Space Sci. 44, 1251–1268.

Mosca, I., Cobden, L., Deuss, A., Ritsema, J., Trampert, J., 2012. Seismic and mineralogical structures of the lower mantle from probabilistic tomography. J. Geophys. Res. 117, B06304. doi:10.1029/2011JB008851.

Mosegaard, K., Tarantola, A., 1995. Monte-Carlo sampling of solutions to inverse problems. J. Geophys. Res. 100, 12431–12447.

Nakamura, Y., 1983. Seismic velocity structure of the lunar mantle. J. Geophys. Res. 88, 677–686.

Nakamura, Y., Latham, G., Dorman, H., Ibrahim, A.B., Koyama, J., Horvarth, P., 1979. Shallow moonquakes - depth, distribution and implications as to the present state of the lunar interior, in: Proc. Lunar Planet. Sci. Conf. 10th, pp. 2299–2309.

Neumann, G., Zuber, M., Wieczorek, M., McGovern, P., Lemoine, F., Smith, D., 2004. Crustal structure of Mars from gravity and topography. J. Geophys. Res. 109, E08002. doi:10.1029/2004JE002262.

Nimmo, F., 2002. Admittance estimates of mean crustal thickness and density at the Martian hemispheric dichotomy. J. Geophys. Res. 107, 5117. doi:10.1029/2000JE001488.

Nimmo, F., Faul, U.H., 2013. Dissipation at tidal and seismic frequencies in a melt-free, anhydrousäâmars. J. Geophys. Res. 118, 2558–2569. doi:10.1002/2013JE004499.

Nimmo, F., Stevenson, D., 2001. Estimates of Martian crustal thickness from viscous relaxation of topography. J. Geophys. Res. 106, 5085–5098.

Okal, E., Sweet, J., 2007. Frequency-size distributions for intraplate earthquakes. GSA Special Papers 425, 59–71.

Phillips, R., 1991. Expected rate of marsquakes, in: Scientifc Rationale and Requirements for a Global Seismic Network on Mars. LPI Tech. Rept., 91-02, Lunar and Planetary Inst., Houston, pp. 35–38.

Phinney, R., 1964. Structure of the Earth's crust from spectral behavior of long-period body waves. J. Geophys. Res. 69, 2997–3017.

Rivoldini, A., Van Hoolst, T., Verhoeven, O., Mocquet, A., Dehant, V., 2011. Geodesy constraints on the interior structure and composition of Mars. Icarus 213, 451–472.

Shapiro, N., Ritzwoller, M., 2002. Monte-Carlo inversion for a global shear-velocity model of the crust and upper mantle. Geophys. J. Int. 151, 88–105.

Shen, W., Ritzwoller, M., Schulte-Pelkum, V., 2013a. A 3-D model of the crust and uppermost mantle beneath the central and western US by joint inversion of receiver functions and surface wave dispersion. J. Geophys. Res. 118, 262–276.

Shen, W., Ritzwoller, M., Schulte-Pelkum, V., Lin, F., 2013b. Joint inversion of surface wave dispersion and receiver functions: a Bayesian Monte-Carlo approach. Geophys. J. Int. 192, 807–836.

Sohl, F., Schubert, G., 2007. Interior structure, composition, and mineralogy of the terrestrial planets, in: Spohn, T., Schubert, G. (Eds.), Treatise on Geophysics. Elsevier. volume 10, pp. 27–68.

Sohl, F., Schubert, G., Spohn, T., 2005. Geophysical constraints on the composition and structure of the Martian interior. J. Geophys. Res. 110, E12008. doi:10.1029/2005JE002520.

Sohl, F., Spohn, T., 1997. The interior structure of Mars: Implications from SNC meteorites. J. Geophys. Res. 102, 1613–1635.

Solomon, S., Anderson, D., Banerdt, W., Butler, R., Davis, P., Duennebier, F., Nakamura, Y., Okal, E., Phillips, R., 1991. Scientific rationale and requirements for a global seismic network on Mars, LPI Tech. Rept. 91-02. Lunar and Planetary Inst., Houston, TX.

Tanimoto, T., Rivéra, L., 2005. Prograde Rayleigh wave particle motion. Geophys. J. Int. 162, 399–405. doi:10.1111/j.1365-246X.2005.02481.x.

Verhoeven, O., Rivoldini, A., Vacher, P., Mocquet, A., Choblet, G., Menvielle, M., Dehant, V., Van Hoolst, T., Sleewaegen, J., Barriot, J.P., Lognonné, P., 2005. Interior structure of terrestrial planets: Modeling Mars' mantle and its electromagnetic, geodetic, and seismic properties. J. Geophys. Res. 110, E04009. doi:10.1029/2004JE002271.

Vinnik, L., Chenet, H., Gagnepain-Beyneix, J., Lognonné, P., 2001. First seismic receiver functions on the Moon. Geophys. Res. Lett. 28, 3031–3034.

Weber, R., Lin, P.Y., Garnero, E., Williams, Q., Lognonné, P., 2011. Seismic detection of the lunar core. Science 331, 309–312.

Wiechert, E., 1910. Bestimmung des weges der Erdbebenwellen im Erdinnern. I. Theroetisches. Phys. Z. 11, 294–304.

Wieczorek, M., Zuber, M., 2004. Thickness of the Martian crust: Improved constraints from geoid-to-topography ratios. J. Geophys. Res. 109, E01009. doi:10.1029/2003JE002153.

Woodhouse, J., 1988. The calculation of eigenfrequencies and eigenfunctions of the free oscillations of the earth and the sun, in: Doornbos, D. (Ed.), Seismological Algorithms. Academic Press, London, pp. 321–370.

Zuber, M., Solomon, S., Phillips, R., Smith, D., Tyler, G., Aharonson, O., Balmino, G., Banerdt, W., Head, J., Johnson, C., Lemoine, F., McGovern, P., Neumann, G., Rowlands, D., Zhong, S., 2000. Internal structure and early thermal evolution of Mars from Mars Global Surveyor topography and gravity. Science 287, 1788–1793.